



Bi₂WO_{6-x} nanosheets with tunable Bi quantum dots and oxygen vacancies for photocatalytic selective oxidation of alcohols



Jinguo Wang*, Hao Liang, Chi Zhang, Bei Jin, Yong Men

College of Chemistry and Chemical Engineering, Shanghai University of Engineering Science, Shanghai, 201620, PR China

ARTICLE INFO

Keywords:
Photocatalysis
Bi₂WO_{6-x}nanosheets
Bi quantum dots
Oxygen vacancy
Selective oxidation

ABSTRACT

Herein, Bi₂WO_{6-x} nanosheets with tunable Bi quantum dots and oxygen vacancies have been synthesized by a facile hydrothermal treatment combining in-situ redox reaction route, which exhibited the highly enhanced activity for selective oxidation of aromatic alcohols to carbonyl compounds in aqueous medium under visible-light irradiation for the first time. Results revealed that the highly enhanced activity of this photocatalyst was mainly attributed to the synergistic effect of Bi quantum dots and oxygen vacancies, which resulted in the narrowed energy band gap by inducing the formation of defect state level below the conduction band, the enhanced light-harvesting ability and the improved separation efficiency of photocharges. Meanwhile, this photocatalyst also displayed excellent durability owing to the strong interaction between Bi quantum dots and robust Bi₂WO_{6-x} nanosheets against significant deactivation caused by either the leaching of Bi quantum dots or the structural collapse of Bi₂WO_{6-x} nanosheets, showing its good potential in practical applications.

1. Introduction

Selective oxidation of alcohols to the value-added carbonyl compounds, generally recognized as one of the most important functional group transformations in organic synthesis, is of vital importance in chemical industry [1–3]. Carbonyl compounds such as aldehydes and ketones are important intermediates or precursors for the synthesis of many drugs, vitamins and fragrances [1–4]. Traditional synthesis of carbonyl compounds is usually achieved by thermal catalysis at high temperature and high pressure in environmentally harmful organic solvents and often catalyzed by employing toxic stoichiometric oxygen oxidants (e.g. Cr, Mn salts or V₂O₅) or moisture-sensitive oxidants [1–5], which not only are expensive and hazardous compounds but also produce large amounts of harmful wastes against the requirements of green chemistry. Therefore, it is highly urgent to develop a clean catalytic process for the efficient synthesis of carbonyl compounds by selective oxidation of alcohols using the environment-benign energy source and green oxidants. As a promising route, semiconductor photocatalysis has been deemed to be an environment-benign and effective technique for pollutant degradation and green organic synthesis [6–12], which is frequently carried out in aqueous medium under mild conditions without using hazardous solvents and oxidants, but its significant challenge is to develop high-efficient semiconductor photocatalysts based on the deep understanding of photocatalytic

mechanism.

Over the past decade, much endeavor has been done to develop high-efficient semiconductor photocatalysts with visible-light responses aiming to utilize solar energy more efficiently. Accordingly, many visible-light-driven semiconductor photocatalysts, mainly including MOF-based photocatalysts [13,14], TiO₂-based photocatalysts doped with metal or nonmetal elements (e.g. Au, Fe, Ag, W, C, N and S) [15–21] and non TiO₂-based photocatalysts (e.g. WO₃, CdS, Ag₃PO₄, g-C₃N₄, Bi₂O₃, BiVO₄, Bi₂MoO₆ and Bi₂WO₆) [9,10,22–28], have been widely explored and applied in heterogeneous photocatalysis. Among them, Bi₂WO₆ with intrinsic narrow energy band gap of 2.70 eV, as a simple Aurivillius oxide and ideal photocatalyst, has received special attention due to its highly stable physicochemical properties and broad applications [28–31], which extends the photoresponse into the visible-light region and thus, makes it more suitable for heterogeneous photocatalysis. However, pure Bi₂WO₆ usually shows the relatively poor photocatalytic performance because of its weak light-harvesting ability and low separation efficiency of photoelectron-hole pairs which in turn limit its future applications [28–32]. In order to alleviate the above problems, many strategies such as nanostructured modulation, doping and heterojunction construction have been employed to endow Bi₂WO₆ with high photocatalytic performance, but its photocatalytic performance is still unsatisfactory owing to the limited amount, easy leaching and uncontrollable spatial distribution of dopants or heterojunctions

* Corresponding author.

E-mail address: Jinguowang1982@sues.edu.cn (J. Wang).

[33–35].

Recent years, the controlled creation of intrinsic defects (e.g. low-valence metal centers or oxygen vacancies) in semiconductor photocatalysts is deemed to be a novel strategy to manipulate their electronic and optical properties and thus, effectively regulate their photocatalytic performances [36–39], which opens up a new era for tailoring the photocatalytic performances of semiconductor photocatalysts. Both theoretical calculations and experimental results have attested that the intrinsic defects, especially the oxygen vacancies, could not only narrow the energy band gap by inducing the formation of defect states below the conduction band and thus, enhance the light-harvesting ability, but also serve as the electron sinks to capture photoelectrons and inhibit their recombination probability with holes and thus, effectively improve the separation efficiency of photoelectron-hole pairs [36–40]. For example, Chai et al. reported that the creation of oxygen vacancies in Bi_2WO_6 led to a greatly enhanced activity for photocatalytic CO_2 reduction [41], and Hou et al. also disclosed that the presence of oxygen vacancies in Bi_2WO_6 played an important role in promoting photocatalytic CO_2 reduction [42]. Wang et al. found that the oxygen vacancies endowed Bi_2WO_6 with highly improved photocatalytic efficiency for the decompositions of rhodamine B and phenol [43], and Zhu et al. proved that the oxygen vacancies increased the photocatalytic activity of Bi_2WO_6 for the degradation of 2, 4-dichlorophenol [44]. Zhang et al. discovered that Bi_2WO_6 with gradient oxygen vacancies exhibited a remarkably enhanced activity for photocatalytic NO oxidation in air atmosphere [45], and Li et al. revealed that the oxygen vacancies in Bi_2WO_6 could significantly improve the photoelectrocatalytic activity for water splitting in near-neutral media [46]. In all above cases, their enhanced photocatalytic performances were generally originated from the controllable creation of oxygen vacancies. Meanwhile, the concept of creating oxygen vacancies has been also reported in other semiconductor photocatalysts such as TiO_2 , ZnO , WO_3 , Fe_2O_3 , BiPO_4 and BiVO_4 [36,37], and all these semiconductor photocatalysts with oxygen vacancies exhibited superior photocatalytic or photoelectrocatalytic performances to their bare counterparts.

Besides the creation of intrinsic defects, the deposition of noble metal particles on semiconductor photocatalysts has been also accepted as an effective strategy to boost their photocatalytic performances. Many studies have revealed that the deposition of noble metal particles (e.g. Au, Pt and Ag) on Bi_2WO_6 led to a great improvement in photocatalytic activity for Cr(VI) reduction, selective oxidation and organic contaminant degradation [47–49], mainly due to the fact that noble metal particles not only enhanced the light-harvesting ability by the plasmonic effect but also acted as the electron receptors to trap photoelectrons and reduce their recombination with holes. Although noble metal particles can drastically enhance the photocatalytic activity of Bi_2WO_6 , the rarity and high cost of noble metals severely limit their practical applications [47–49]. As a promising candidate, metallic bismuth (Bi) can be considered as a suitable substitute because of its low cost and outstanding plasmonic effect [50–52]. For instance, both Li's group and Huang's group have revealed that the deposition of metallic Bi particles on Bi_2WO_6 greatly improved the photocatalytic activity for organic contaminant degradations due to the plasmonic effect of metallic Bi particles [51,52]. Accordingly, the plasmonic effect of metallic Bi particles has been successfully extended into other semiconductor photocatalysts such as TiO_2 , Bi_2O_3 , BiOCl and $(\text{BiO})_2\text{CO}_3$ [53–56], and all these metallic Bi particles depositing semiconductor photocatalysts exhibited higher photocatalytic performances than their bare counterparts. Despite considerable efforts have been paid to accomplish Bi_2WO_6 with highly improved photocatalytic performances by creating oxygen vacancies or depositing Bi particles for organic contaminant degradation, hydrogen production by water splitting, photocatalytic NO oxidation and photocatalytic CO_2 reduction, the simultaneous generation of oxygen vacancies and metallic Bi particles on Bi_2WO_6 for selective organic transformations has been seldom reported so far.

Meanwhile, further researches are extremely needed to reveal the essential promoting mechanism of oxygen vacancies and metallic Bi particles on the photocatalytic performances.

Herein, $\text{Bi}_2\text{WO}_{6-x}$ nanosheets with tunable Bi quantum dots and oxygen vacancies have been successfully synthesized by a facile hydrothermal treatment combining in-situ redox reaction route. To the best of our knowledge, this is the first study reporting on the simultaneous generation of Bi quantum dots and oxygen vacancies on $\text{Bi}_2\text{WO}_{6-x}$ nanosheets for selective alcohol oxidations in aqueous medium under visible-light irradiation. Results revealed that this photocatalyst exhibited the highly enhanced activity due to the synergistic effect of Bi quantum dots and oxygen vacancies, which resulted in the enhanced light-harvesting ability, the narrowed energy band gap and the improved separation efficiency of photoelectron-hole pairs. Meanwhile, this photocatalyst also showed excellent durability owing to the strong interaction between Bi quantum dots and robust $\text{Bi}_2\text{WO}_{6-x}$ nanosheets against either the leaching of Bi quantum dots or the structural collapse of $\text{Bi}_2\text{WO}_{6-x}$ nanosheets. Moreover, the photocatalytic mechanism of selective alcohol oxidations has been proposed and elaborated in details on the basis of active species identified by capturing experiments. We believe that the findings from this study can deliver some new insights for guiding the rational design of high-efficient photocatalysts applied in the field of green and sustainable organic transformations.

2. Experimental

2.1. Catalyst synthesis

The chemical reagents employed in present work were of analytical grade and used without further treatment. Bi_2WO_6 nanosheets were synthesized by a slightly modified hydrothermal route according to the previous study [48]. Briefly, 1.94 g $\text{Bi}(\text{NO}_3)_3 \cdot 5\text{H}_2\text{O}$ was added into a 140 mL aqueous solution containing 0.66 g $\text{Na}_2\text{WO}_6 \cdot 2\text{H}_2\text{O}$ and 0.10 g hexadecyl trimethyl ammonium bromide under magnetic stirring until forming a homogeneous suspension, and then the suspension was poured into a 200 mL Teflon-lined autoclave and kept at 120 °C for 24 h. Afterwards, the precipitates were collected and thoroughly washed with distilled water, and then dried at 80 °C for 10 h in air to obtain the Bi_2WO_6 nanosheets, which was denoted as BWO.

$\text{Bi}_2\text{WO}_{6-x}$ nanosheets with tunable Bi quantum dots and oxygen vacancies were prepared by a facile in-situ redox reaction between Bi_2WO_6 and reductive NaBH_4 aqueous solution. Typically, 20 mL NaBH_4 solution with different molar concentrations (1.0 mM, 2.0 mM, 2.5 mM, 5.0 mM and 10 mM) was slowly added into a white suspension containing 0.50 g BWO and 20 mL distilled water under the high-purity N_2 atmosphere. After stirring for 10 min at room temperature, the precipitates were collected and thoroughly washed with distilled water for four times, and then dried at 60 °C for 10 h in a vacuum oven to obtain the final products. The final products were denoted as XBWO, where X referred to the molar concentration of NaBH_4 aqueous solution.

2.2. Characterization

The morphological structures characterized by field emission scanning electron microscopy (FESEM) and high-resonance transmission electron microscopy (HRTEM) were captured on Hitachi S4800 and JEOL JEM-2100 with the accelerating voltages of 5.0 kV and 200 kV, respectively. N_2 sorption isotherms collected on Micromeritics ASAP 2460 at the temperature of 77 K were applied to calculate the surface area (S_{BET}), pore volume (V_p) and pore diameter (D_p) by using Brunauer-Emmett-Teller (BET) and Barrett-Joyner-Halenda (BJH) models from the desorption branches. The crystal structure determined by X-ray diffraction (XRD) was conducted on Rigaku D/Max-2000 using monochromatic $\text{CuK}\alpha$ radiation in the 2θ value range of 25–60° operated at 40 kV and 30 mA. Raman spectra and photoluminescence

spectroscopy (PLS) were achieved on Dilor Super LabRam II and Varian Cary-Eclipse 500 with the excitation wavelengths of 633 nm and 300 nm, respectively. Electron paramagnetic resonance (EPR) analysis was performed on a JEOL JES-FA200 spectrometer without light irradiation at the temperature of 77 K. The surface electronic states analyzed by X-ray photoelectron spectroscopy (XPS) were taken on Escalab 250Xi and all the binding energy values were calibrated by using the reference of $C_{1s} = 284.6$ eV. UV-vis diffuse reflectance spectra (UV-vis DRS) was recorded on MC-2530 by using 100% BaSO_4 as a reflectance standard. The photocurrent response recorded on an electrochemical system (CHI-660E, China) was carried out in a conventional three-electrode quartz cell containing 0.50 M Na_2SO_4 aqueous solution, and the system coupled with a 300 W Xe arc lamp was irradiated by full wavelengths. The Ag/AgCl electrode and Pt foil were used as the reference and counter electrodes, respectively, while the work electrode was prepared by depositing 10 mg photocatalyst onto the fluoride-tin oxide (FTO) conductor glass. The products of selective alcohol oxidations were qualitatively identified and analyzed by GC-MS (Agilent 6890N/5973I).

2.3. Photocatalytic activity evaluation

The selective oxidation of alcohols by heterogeneous photocatalysis was performed in a self-designed 100 mL reactor (see Fig. S1) containing 0.10 g photocatalysts, 10 mL H_2O and 0.10 mmol aromatic alcohols (e.g. benzyl alcohol, 1-phenylethanol or their derivatives) at 25 °C. All the reactions were carried out in a static O_2 atmosphere (1.0 atm) and stirred for 1.0 h to make the photocatalysts blend evenly in the solution, and then the reactions were initiated by irradiating with a 300 W Xe arc lamp coupled with a 420 nm cut-off filter at 15 cm away from the solution. After reacting 6.0 h, the reaction products were extracted with diethyl ether and quantitatively analyzed by using gas chromatograph (Shimadzu, GC-2014). The blank experiments indicated that no measurable alcohol oxidations happened in the absence of either light irradiation or photocatalysts. The active species identified by capturing experiments were conducted using the same method by charging 40 mmol of different scavengers. The reproducibility of all the activity data was achieved by repeating each result at least three times and found to be within acceptable levels ($\pm 3.0\%$).

3. Results and discussion

3.1. Physicochemical characteristics

The FESEM images in Fig. 1 display that all the prepared catalysts were present in typically two-dimensional nanosheets with an average

length of *ca.* 700 nm and an ultrathin thickness less than 10 nm. Notably, it can be seen that no visual effect on the morphological structures of all the XBWO catalysts was observed by the in-situ reduction treatment using different molar concentrations of NaBH_4 aqueous solution in comparison with BWO. Meanwhile, the TEM images in Fig. 2 demonstrate the consistent morphology and corresponding size distribution of all the prepared catalysts as disclosed by FESEM analysis. The TEM images also reveal that the worm-like mesopores were existed in all the prepared catalysts, mainly resulting from the aggregated voids by the self-assembly of the nanoparticle units [57–59]. The attached SAED images indicated that all the prepared catalysts possessed the polycrystalline structure with high crystallization degree as evidenced by the bright diffraction rings. The reflections with the *d*-spacing values of 0.32 nm and 0.24 nm in the HRTEM image of 2.5BWO were assigned to the principal (131) facet of the orthorhombic Bi_2WO_6 crystal phase and the (104) facet of metallic Bi with the rhombohedral crystal phase [48,50], respectively. Interestingly, the metallic Bi particles were well separated from each other and spread out on the surface of nanosheets, and the size of metallic Bi particles increased gradually in the range of 4.0–10 nm from 2BWO to 10BWO with increasing the molar concentration of NaBH_4 aqueous solution. This appearance was attributed to the fact that the increase in the molar concentration of NaBH_4 aqueous solution could reduce more Bi^{3+} cations in Bi_2WO_6 nanosheets to generate metallic Bi particles. However, it should be pointed out that no metallic Bi particles could be found in 1BWO, possibly ascribing to its low amount and extremely small size of metallic Bi particles.

The XRD patterns in Fig. 3 show that all the prepared catalysts were present in orthorhombic Bi_2WO_6 crystal phase with the characteristic diffraction peaks at the 2θ values of 28.3°, 32.8°, 47.1° and 56.0° corresponding to the (131), (200), (202) and (133) facets (JCPDS Card No. 39-0256) [47–49], respectively. Notably, no characteristic diffraction peaks featured to the metallic Bi particles were observed in all the XBWO catalysts, mainly due to their low amounts and high dispersion of metallic Bi particles. Meanwhile, the characteristic diffraction peaks of all the prepared catalysts became slightly weaken and broaden with the increase in the molar concentration of NaBH_4 aqueous solution during the in-situ reduction process, suggesting the gradual decrease in the crystallization degree, which was in good accordance with the previous studies [39,60]. Based on the principal (131) peaks of all the prepared catalysts, the crystalline size has been calculated by using Scherrer's equation. As shown in Table 1, the crystalline size of all the prepared catalysts decreased gradually from 9.3 nm to 7.2 nm with increasing the molar concentration of NaBH_4 aqueous solution during the in-situ reduction process, further confirming the gradual decrease in the crystallization degree. Besides, from the enlarged 2θ value range of 32–34° in Fig. 3b, it can be clearly seen that the (200) peak position of

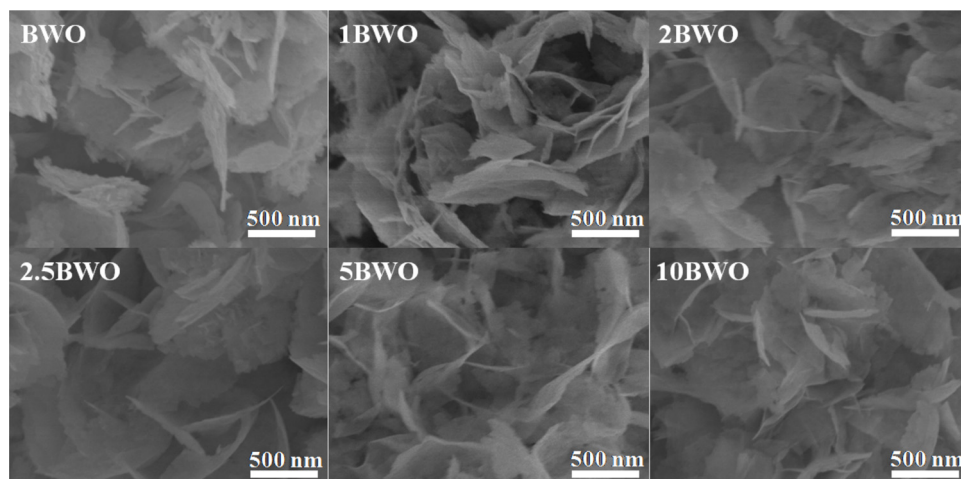


Fig. 1. FESEM images of different catalysts.

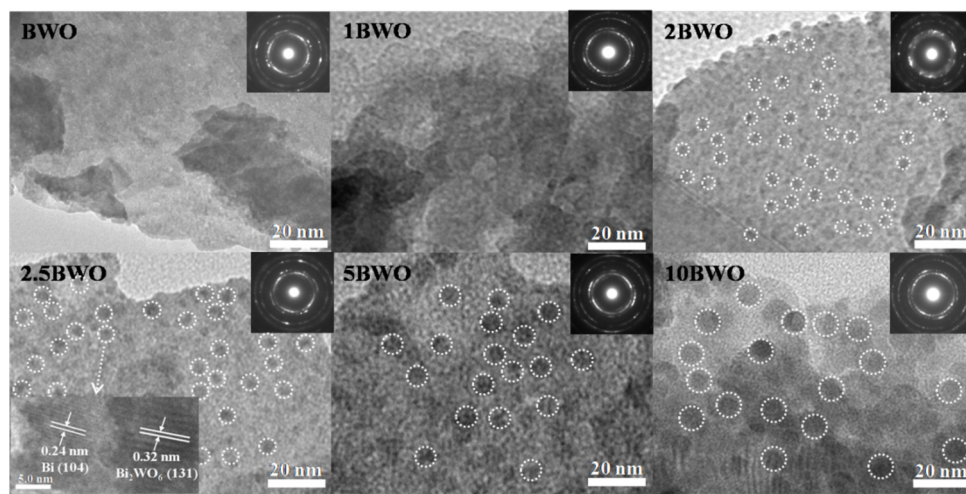


Fig. 2. TEM, HRTEM and SAED (inset) images of different catalysts.

all the XBWO catalysts red-shifted slightly to the high angle with increasing the molar concentration of NaBH_4 aqueous solution as compared with BWO, which was mainly caused by the residual stress coming from the generation of oxygen vacancies that resulted in the lattice shrinkage [39,46,60].

To identify the generation of oxygen vacancies in all the XBWO catalysts, the Raman technique has been employed to characterize all the prepared catalysts as shown in Fig. 4a. It can be obviously seen that all the prepared catalysts presented four major peaks located at about 304 cm^{-1} , 717 cm^{-1} , 796 cm^{-1} and 829 cm^{-1} , agreeing well with the previously reported researches [41,60,61]. The peak centered at around 304 cm^{-1} was assigned to the translation modes that involved the simultaneous motions of Bi^{3+} and WO_6^6- , whereas the peak located at about 717 cm^{-1} could be indexed to the tungstate chain antisymmetric bridging mode [41,60]. The strong peaks at about 796 cm^{-1} and 829 cm^{-1} represented the antisymmetric and symmetric A_g stretching modes of terminal O–W–O groups [42,61], respectively. All the other peaks in the range of 200 – 520 cm^{-1} were associated with the bending and stretching vibrations of BiO_6 polyhedron, WO_6 octahedron and Bi –O bands [41]. Meanwhile, the full width at half-maximum value of these four major peaks for all the XBWO catalysts increased gradually with the increase in the molar concentration of NaBH_4 aqueous solution as compared with BWO, signifying the increased number of oxygen

vacancies on the surface of all the XBWO catalysts from 1BWO to 10BWO. This fact also further manifested that the decrease in crystallization degree of all the XBWO catalysts resulted from the generation of oxygen vacancies. Moreover, the EPR spectra in Fig. 4b provided direct evidences to further confirm the generation of oxygen vacancies in all the XBWO catalysts. Compared with BWO, all the XBWO catalysts exhibited a sharp EPR signal centered at around $g = 1.999$, which was assigned to the Zeeman effect of the unpaired electrons trapped at the sites of oxygen vacancies [42,60], distinctly verifying the generation of oxygen vacancies in all the XBWO catalysts. Furthermore, as previously reported researches, the number or concentration of oxygen vacancies can be proportional to the peak intensity of EPR signal [39,45]. It can be noted that the peak intensity of EPR signals increased gradually in all the XBWO catalysts from 1BWO to 10BWO, indicating the increase in the number of oxygen vacancies.

The surface chemical compositions and chemical valence states of all the prepared catalysts have been investigated by XPS technique as shown in Fig. 5. The survey spectra in Fig. S2 revealed that all the prepared catalysts only contained the Bi, O and W elements and no other impurities were found, implying the high purity of all the prepared catalysts. The high-resolution $\text{Bi}4f$ spectrum of all the prepared catalysts in Fig. 5a exhibited two major spin-orbit doublets with the $\text{Bi}4f_{7/2}$ and $\text{Bi}4f_{5/2}$ corresponding to the binding energies at about

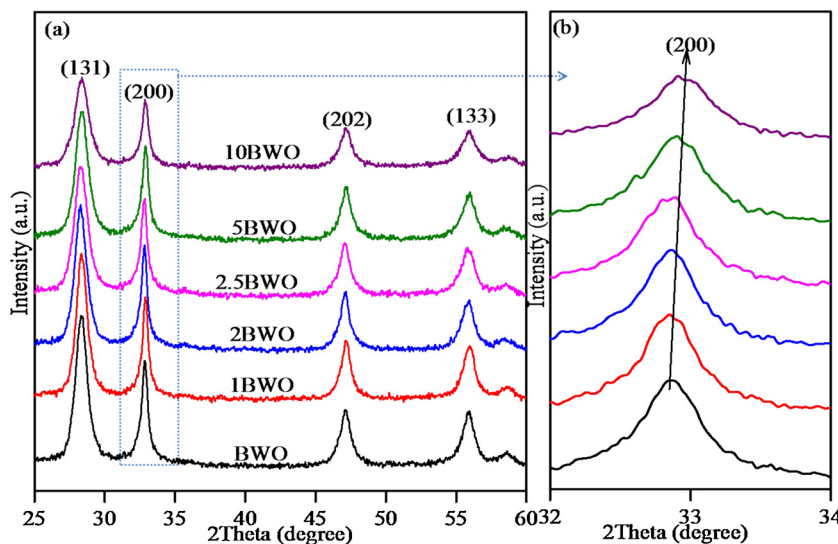


Fig. 3. XRD patterns (a) and the magnified 32 – 34° range (b) of different catalysts.

Table 1
Physicochemical structural parameters of different catalysts.

Catalyst	S_{BET} (m^2/g)	V_p (cm^3/g)	D_p (nm)	Crystalline size (nm)	XPS envelope		
					W^{5+}/W^{6+}	$\text{Bi}^0/\text{Bi}^{3+}$	O_{ads}/O_L
BWO	34	0.14	14	9.3	0.042	0.029	0.10
1BWO	34	0.14	14	8.3	0.082	0.031	0.16
2BWO	37	0.16	15	8.2	0.091	0.036	0.19
2.5BWO	41	0.17	14	8.0	0.102	0.044	0.20
5BWO	42	0.16	14	7.6	0.110	0.051	0.22
10BWO	37	0.14	16	7.2	0.121	0.060	0.24

159.2 eV and 164.6 eV [41,51,61], respectively. The signals of Bi^{3+} cations and metallic Bi^0 were observed after the deconvolution of $\text{Bi}4f$ spectra by using Gaussian fitting methods. The two distinct peaks corresponding to the binding energies at about 159.4 eV and 164.8 eV were assigned to the characteristic Bi^{3+} cations while two other small peaks with the binding energies at about 157.9 eV and 163.2 eV were linked to the low-valence state of metallic Bi^0 [51,62]. Notably, the binding energy of Bi species for all the XBWO catalysts blue-shifted slightly to the higher binding energy as compared with BWO, mainly owing to the formation of neighbouring oxygen vacancies with higher electron attracting ability [41]. The high-resolution $W5f$ spectrum of all the prepared catalysts in Fig. 5b showed two strong peaks corresponding to the $W4f_{7/2}$ at the low binding energy of 35.4 eV and the $W4f_{5/2}$ at the high binding energy of 37.6 eV [10,41,42]. The signals of W^{5+} and W^{6+} cations can be found after the decomposition of $W4f$ spectra. The peaks of $W4f$ at the binding energies around 34.7 eV and 36.9 eV were indexed to the low oxidation state of characteristic W^{5+} cations, whereas the peaks of $W4f$ at the binding energies about 35.5 eV and 37.7 eV were featured to the high oxidation state of typical W^{6+} cations [10,42,62]. The presence of W^{5+} cations is usually connected to the generation of oxygen vacancies. To elucidate the origin of oxygen vacancies, the high-resolution O1s spectrum of all the prepared catalysts in Fig. 5c has been decomposed into two major peaks at the binding energies of 530.1 eV and 531.7 eV, corresponding to the lattice oxygen (O_L) species and surface chemisorbed oxygen (O_{ads}) species (e.g. O_2^{2-} , O_2^- , OH^- or O^-) [10,63], respectively. As previously reported

study [41], the generation and concentration of oxygen vacancies could be reflected by the peak intensity of surface chemisorbed oxygen (O_{ads}) species. Clearly, the peak intensity of O_{ads} in Fig. 5c increased slightly from BWO to 10BWO, indicating the increased number of oxygen vacancies. Based on the XPS analysis, the quantified surface chemical compositions and chemical valence states of all the prepared catalysts have been calculated and summarized in Table 1. It was obvious that the molar ratios of $\text{Bi}^0/\text{Bi}^{3+}$ and W^{5+}/W^{6+} for all the prepared catalysts increased gradually from BWO to 10BWO, mainly due to the fact that the increase in the molar concentration of NaBH_4 aqueous solution enhanced the reductive ability and thus, made the reductions of Bi^{3+} to metallic Bi^0 and W^{6+} to W^{5+} more easily. Meanwhile, the molar ratio of O_{ads}/O_L also increased gradually from BWO to 10BWO, corresponding to the increase in the number of oxygen vacancies, which was in good agreement with the results as revealed by Raman and EPR analysis. This appearance was attributed to the reason that the generation of oxygen vacancies was mainly contributed by the reductions of Bi^{3+} to metallic Bi^0 and W^{6+} to W^{5+} in Bi_2WO_6 nanosheets.

The N_2 sorption isotherms in Fig. 6 display that all the prepared catalysts presented the typical type-IV N_2 adsorption-desorption isotherms with a small H1 hysteresis loop in the relative pressure (P/P_0) range of 0.7–1.0, suggesting the presence of typical mesoporous structures in all the prepared catalysts that were usually associated with the slit-shaped pores according to the IUPAC classifications [57,64,65]. The presence of slit-shaped pores in all the prepared catalysts generally resulted from the sheet-like feature, agreeing well with their FESEM

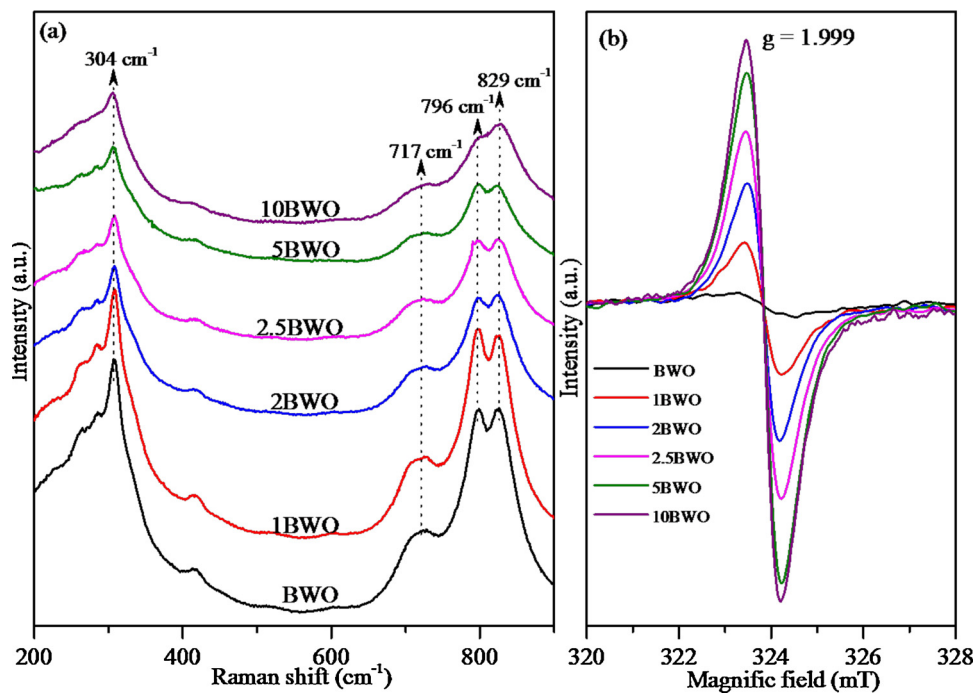


Fig. 4. Raman spectra (a) and EPR spectra (b) of different catalysts.

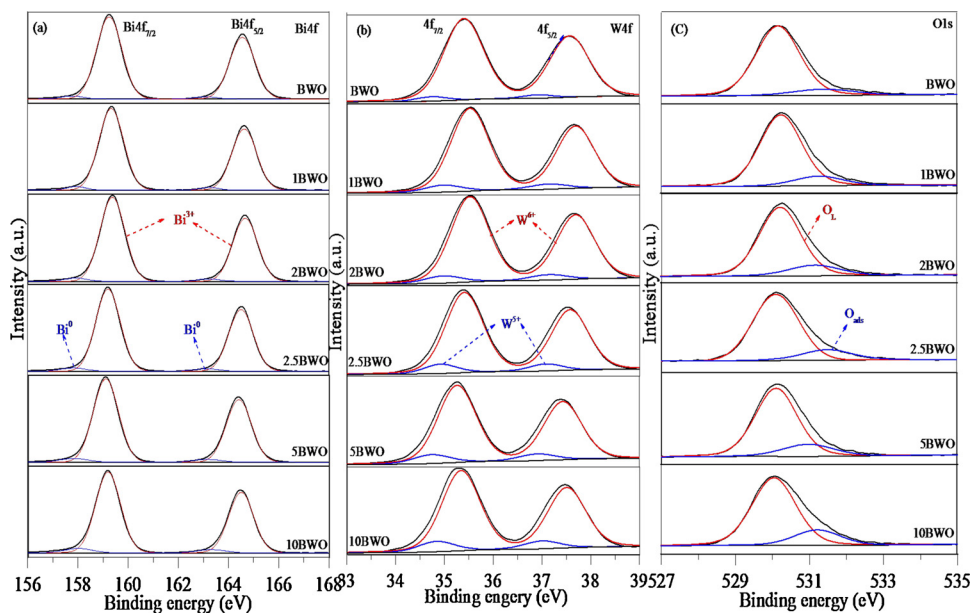


Fig. 5. XPS spectra of different catalysts: Bi4f of (a), W4f of (b) and O1s of (c).

and TEM analysis. Meanwhile, this speculation can be evidenced by their pore size distribution curves in which a wide pore size distribution can be observed in the range from 2.0 nm to 30 nm. The small mesopores centered at around 4.0 nm was mainly originated from the aggregated voids by the self-assembly of the nanoparticle units while the large mesopores in the range of 5.0–30 nm could be attributed to the self-assembly of nanosheet-like units [57,64]. Based on the N₂ sorption isotherms, the specific surface area (S_{BET}), pore volume (V_p) and pore size (D_p) of all the prepared catalysts have been calculated by using BET and BJH models from the desorption branches, respectively. From Table 1, it can be noticed that the S_{BET} of all the prepared catalysts increased slightly from BWO to 5BWO with increasing the molar concentration of NaBH₄ aqueous solution in the range of 1.0–5.0 mM. This

phenomenon can be ascribed to the gradual decrease in the crystalline size, which resulted from the increase in the molar concentration of NaBH₄ aqueous solution decreasing the crystallization degree of all the prepared catalysts as revealed by XRD analysis. However, further increase in the molar concentration (10 mM) of NaBH₄ aqueous solution resulted in the decreased surface area of 10BWO although it had the smallest crystalline size, which can be mainly due to the occupation of large Bi particles in the small mesopores.

The photocurrent response of all the prepared catalysts has been also studied under visible-light irradiation as shown in Fig. 7. It can be seen that the photocurrent response of all the prepared catalysts generated immediately when the visible-light irradiation was turned on, and then decayed rapidly to zero once the visible-light irradiation was

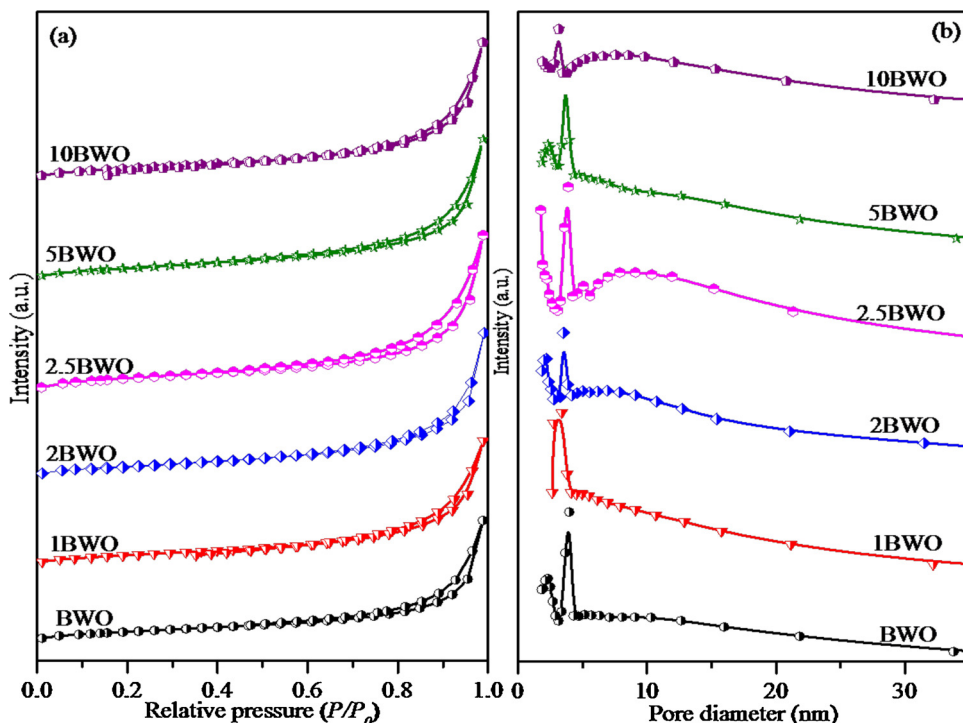


Fig. 6. N₂ adsorption-desorption isotherms (a) and pore size distribution curves (b) of different catalysts.

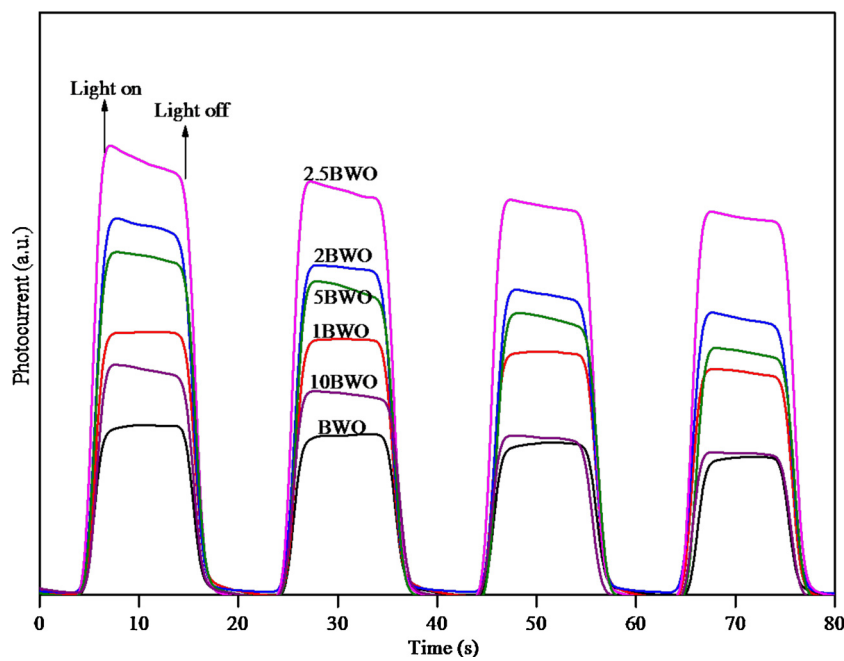
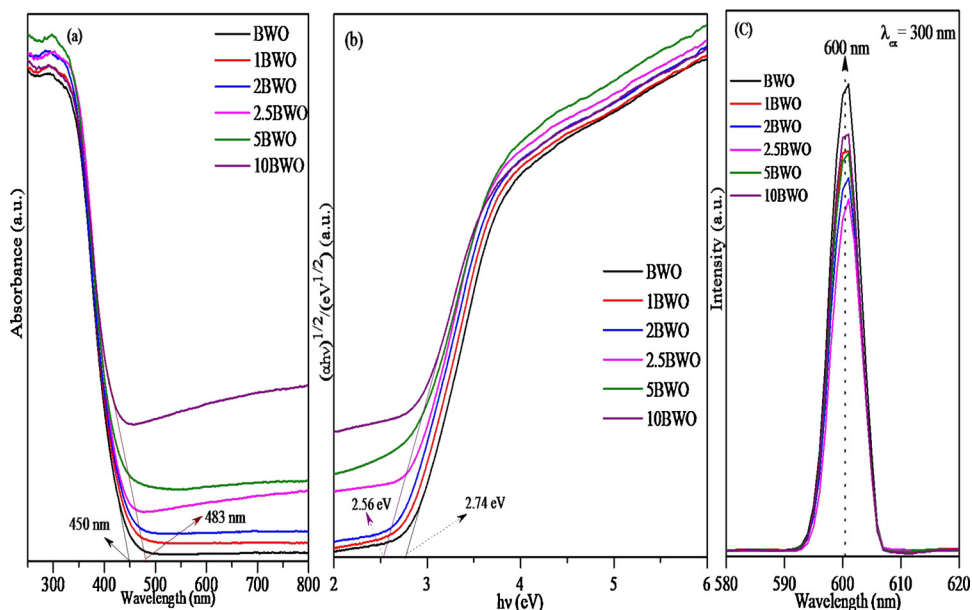


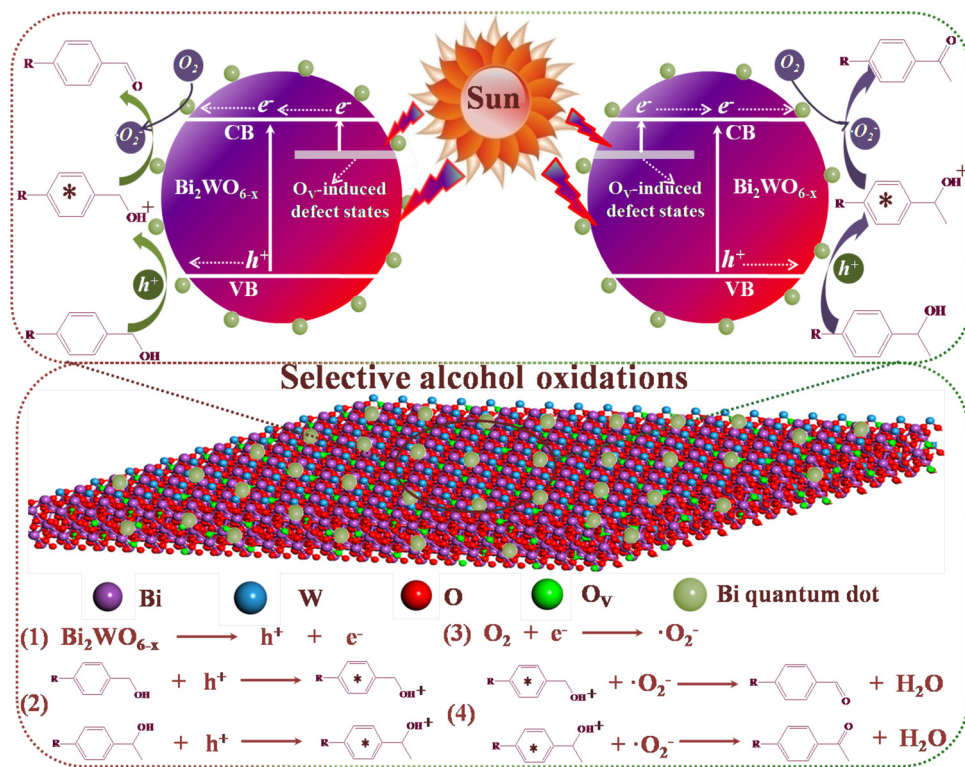
Fig. 7. Photocurrent response of different catalysts.

turned off, attesting that all the prepared catalysts functioned as the semiconductors to produce photoelectrons under visible-light irradiation. Notably, the photocurrent intensity initially increased from BWO to 2.5BWO, and then decreased gradually from 2.5BWO to 10BWO. Therefore, the 2.5BWO was identified as the catalyst with the highest photocurrent intensity under present conditions, signifying that it owned the highest separation efficiency of photoelectron-hole pairs [8–10]. Generally, the photocurrent intensity is dependent on the light-harvesting ability and the separation efficiency of photoelectron-hole pairs [8–10]. Thus, the highest photocurrent intensity of 2.5BWO can be associated with the two major factors as follows.

On the one hand, the light-harvesting ability of all the prepared catalysts has been investigated by using the UV-vis DRS technique as shown in Fig. 8a. It can be seen that the BWO exhibited the absorption edge at around 450 nm, while the absorption edge within the visible-

light range for all the XBWO catalysts apparently red-shifted to 483 nm, indicating the enhancement in the light-harvesting ability and the narrowing in the energy band gap [39,41,46,61]. The energy band gap of all the prepared catalysts has been estimated by employing Kubelka-Munk function through the equation of $(ahv)^n = c(hv - E_g)$, where the a , v , h , c , E_g and n referred to the absorption coefficient, the light frequency ($3.0 \times 10^8 \text{ m} \cdot \text{s}^{-1}$), the Planck's constant ($4.136 \times 10^{-15} \text{ eV} \cdot \text{s}$), a constant ($c = 1$), the energy band gap and the indirect gap semiconductor ($n = 1/2$) [45,60,61], respectively. From Fig. 8b, the energy band gap of BWO calculated at about 2.74 eV is higher than the theoretical value of 2.70 eV [28–31], which can be mainly attributed to the nanoscale effect of its ultrathin nanosheets. Meanwhile, it was obvious that the approximated energy band gap of all the prepared catalysts from BWO to 10BWO decreased slightly from 2.74 eV to 2.56 eV, confirming the narrowing in the energy band gap. This band gap narrowing

Fig. 8. UV-vis DRS spectra (a), the $(ohv)^{1/2}$ versus $h\nu$ plots (b) and PLS spectra (c) of different catalysts.



Scheme 1. Photocatalytic mechanism for selective oxidation of aromatic alcohols to their corresponding aldehydes or ketones over 2.5BWO.

can be ascribed to the formation of oxygen vacancies (O_v) induced defect states below the conduction band as depicted in **Scheme 1**, which extended the photoresponse in the visible-light range and made use of more visible lights, thereby favoring the enhanced light-harvesting ability [41,46]. Moreover, it can be seen that a considerably large absorption tail in the visible-light range of 470–800 nm for all the XBWO catalysts was observed as compared with BWO, which was mainly originated from the plasmonic effect of metallic Bi particles and the generation of oxygen vacancies that also improved the light-harvesting ability [10,51,66]. The intensity of the absorption tail for all the XBWO catalysts increased dramatically from 1BWO to 10BWO, implying the increased amounts of metallic Bi particles and oxygen vacancies in good compliance with the results revealed by Raman, EPR and XPS characterizations. Furthermore, the increased specific surface area of all the XBWO catalysts was also responsible for the enhanced light-harvesting ability as compared with BWO, because of that the increased surface area could enlarge the contact area between photocatalysts and lights and benefit the enhanced light-harvesting ability.

On the other hand, the separation efficiency of photoelectron-hole pairs for all the prepared catalysts has been evaluated by using the PLS analysis as shown in **Fig. 8c**. Clearly, the intensity of PL emission peak centered at around 600 nm decreased greatly from BWO to 2.5BWO corresponding to the improved separation efficiency of photoelectron-hole pairs [8–10], and then increased gradually from 2.5BWO to 10BWO indicative of the increased recombination rate of photoelectron-hole pairs [64], which agreed well with the variation in the photocurrent intensity (see **Fig. 7**). Thus, the 2.5BWO was recognized as the catalyst with the highest separation efficiency of photoelectron-hole pairs. The improved separation efficiency of photoelectron-hole pairs from BWO to 2.5BWO can be ascribed to the factor that the decrease in crystalline size could shorten the transfer distance of photoelectrons and favor the fast transfer of photoelectrons and thus, effectively reduce their recombination probability with holes [8,9,64,67]. Meanwhile, the increase in the amounts of metallic Bi particles and oxygen vacancies also accounted for the improved separation efficiency of photoelectron-hole pairs owing to the fact that both metallic Bi particles and oxygen

vacancies can serve as the electron sinks to trap photoelectrons and inhibit their recombination with holes, thereby promoting the separation of photoelectrons from holes [37,38,51,52]. However, both 5BWO and 10BWO also displayed the lower separation efficiency of photoelectron-hole pairs than that of 2.5BWO although they had smaller crystalline size and higher amounts of metallic Bi particles and oxygen vacancies, mainly due to the reason that their excess amounts of metallic Bi particles and oxygen vacancies became the recombination centers for the photoelectron-hole pairs which in turn suppressed their separation from each other [37,38].

3.2. Photocatalytic performances

Selective oxidation of aromatic alcohols to carbonyl compounds by semiconductor photocatalysis has been selected as the model reaction to evaluate the photocatalytic activities of all the prepared catalysts. Prior to the photocatalytic evaluation, the photocatalytic reaction mechanism for selective oxidation of aromatic alcohols to carbonyl compounds was initially studied over 2.5BWO by using benzyl alcohol and 1-phenylethanol as the typical aromatic alcohols on the basis of active species identified by capturing experiments. Meanwhile, blank experiments indicated that no measurable amounts of oxidation products for benzyl alcohol and 1-phenylethanol could be detected in the absence of either visible-light irradiation or photocatalyst, and the GC-MS analysis revealed that no side-products other than carbonyl compounds for selective oxidation of benzyl alcohol and 1-phenylethanol could be found, suggesting the absolute selectivity towards the target carbonyl compounds under present conditions. From **Fig. 9**, it can be seen that no significant change in photocatalytic activities for selective oxidation of benzyl alcohol and 1-phenylethanol was observed when the terephthalic acid was added into the reaction systems to capture the hydroxyl radicals ($\cdot\text{OH}$), indicating that the $\cdot\text{OH}$ radicals were not the key active species involved in the photocatalytic selective alcohol oxidations under present conditions [8–10,67,68]. However, great decreases in photocatalytic activities regardless of selective oxidation of benzyl alcohol or 1-phenylethanol were found by adding either methanol to

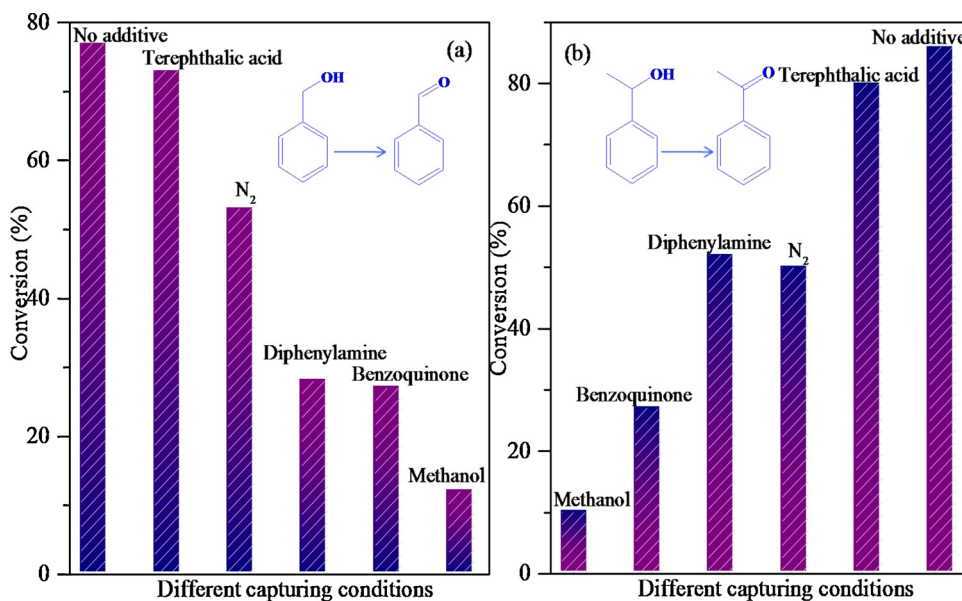


Fig. 9. Photocatalytic performances for selective oxidation of benzyl alcohol (a) and 1-phenylethanol (b) in the presence of different capturers over 2.5BWO.

capture the photogenerated holes (h^+), or benzoquinone to capture the superoxide radicals ($\cdot O_2^-$), or diphenylamine to capture the photoelectrons (e^-), or bubbling high-purity N_2 atmosphere into the reaction solution to eliminate the dissolved O_2 [8–10,67]. These results afforded powerful evidences that, except for the hydroxyl radicals ($\cdot OH$), both the photogenerated holes (h^+) and the photoelectrons (e^-) together with the superoxide radicals ($\cdot O_2^-$) were mainly engaged as the key active species involved in the photocatalytic selective alcohol oxidations under present conditions. Based on the above results, a plausible photocatalytic reaction mechanism for selective oxidation of aromatic alcohols to carbonyl compounds was proposed and briefly depicted in Scheme 1 and Eq. 1–4. Firstly, the Bi_2WO_{6-x} nanosheets produced the photogenerated holes (h^+) and the photoelectrons (e^-) under visible-light irradiation (Eq. 1). Then, the photogenerated holes (h^+) activated the aromatic alcohol molecules of benzyl alcohol or 1-phenylethanol absorbed on the surface of Bi_2WO_{6-x} nanosheets to produce the corresponding benzyl alcohol cation radicals ($\cdot \text{C}_6\text{H}_4\text{CH}_2\text{OH}^+$) or 1-phenylethanol cation radicals ($\cdot \text{C}_6\text{H}_4\text{CH}_2\text{CH}_3^+$) (Eq. 2). The photoelectrons (e^-) initially jumped from the valence band and the O_V -induced defect states to the conduction band, and then transferred to the metallic Bi particles and subsequently reacted with the dissolved O_2 in the reaction solution to generate the superoxide radicals ($\cdot O_2^-$) (Eq. 3). Lastly, the benzyl alcohol cation radicals ($\cdot \text{C}_6\text{H}_4\text{CH}_2\text{OH}^+$) or 1-phenylethanol cation radicals ($\cdot \text{C}_6\text{H}_4\text{CH}_2\text{CH}_3^+$) reacted with the superoxide radicals ($\cdot O_2^-$) to produce the corresponding carbonyl compounds (Eq. 4).

The photocatalytic activities of all the prepared catalysts for selective oxidation of benzyl alcohol and 1-phenylethanol to their corresponding aldehyde and ketone, respectively, were shown in Fig. 10. Obviously, it can be seen that the photocatalytic activities, regardless of selective oxidation of benzyl alcohol or 1-phenylethanol, firstly increased dramatically from BWO to 2.5BWO and then decreased gradually from 2.5BWO to 10BWO. Hence, the 2.5BWO was undeniably considered as the optimal photocatalyst for selective oxidation of benzyl alcohol and 1-phenylethanol under present conditions. The superior photocatalytic activity of 2.5BWO was mainly attributed to the synergistic effect of the following crucial factors. Firstly, the increase in surface area (see Table 1) not only favored the adsorption and diffusion of aromatic alcohol molecules but also enlarged the contact area between photocatalysts and lights and thus, improved the light-harvesting ability. Secondly, the metallic Bi particles favored the enhanced light-harvesting ability by the plasmonic effect, and the oxygen vacancies

resulted in the energy band gap narrowing by the formation of oxygen vacancies induced defect state levels below the conduction band, which extended the potoresponse in the visible-light range and utilized the visible lights more efficiently, thereby greatly enhancing the light-harvesting ability. Thirdly, both metallic Bi particles and oxygen vacancies could serve as the electron sinks to capture photoelectrons and effectively inhibit their recombination probability with photogenerated holes and thus, promote the improved separation efficiency of photoelectron-hole pairs. Meanwhile, many previous studies have attested that the oxygen vacancies with abundant localized electrons could act as the active sites for the adsorption and activation of reactant molecules, and the surface catalytic reactions could be initiated once the reactant molecules adsorbed onto the sites of oxygen vacancies [37–40], which might be also the important reason for the superior photocatalytic activity of 2.5BWO. Finally, the small crystalline size could effectively shorten the transfer distance of photoelectrons and facilitate the fast transfer of photoelectrons and thus, efficiently promote their separation from holes. Moreover, the BWO and 1BWO together with 2BWO showed weaker photocatalytic activities than 2.5BWO, mainly ascribing to the factors that their lower surface area restricted the adsorption and diffusion of alcohol molecules, their larger crystalline size increased the recombination probability of photoelectron-hole pairs, and their lower amounts of metallic Bi particles and oxygen vacancies resulted in the weaker light-harvesting ability and lower separation efficiency of photoelectron-hole pairs (see Fig. 8). Furthermore, both 5BWO and 10BWO also demonstrated weaker photocatalytic activities than that of 2.5BWO although they had smaller crystalline size, higher light-harvesting ability and higher amounts of metallic Bi particles and oxygen vacancies. This fact could be associated with the reason that their excess amounts of metallic Bi particles and oxygen vacancies became the recombination centers for photoelectron-hole pairs and inhibited their separation from each other, thereby decreasing the separation efficiency of photoelectron-hole pairs (see Fig. 8c).

The substituent effect of aromatic alcohols on the photocatalytic activity has been explored over 2.5BWO as shown in Fig. 11. Clearly, it can be found that the substituent effect of aromatic alcohols, regardless of benzyl alcohol or 1-phenylethanol, played an important role in determining the photocatalytic activity of 2.5BWO. The aromatic alcohols with electron-donating groups (e.g. *p*-CH₃ and *p*-OCH₃) displayed higher photocatalytic activities than those with electron-withdrawing groups (e.g. *p*-F, *p*-Cl, *p*-Br and *p*-NO₂), which agreed well with the

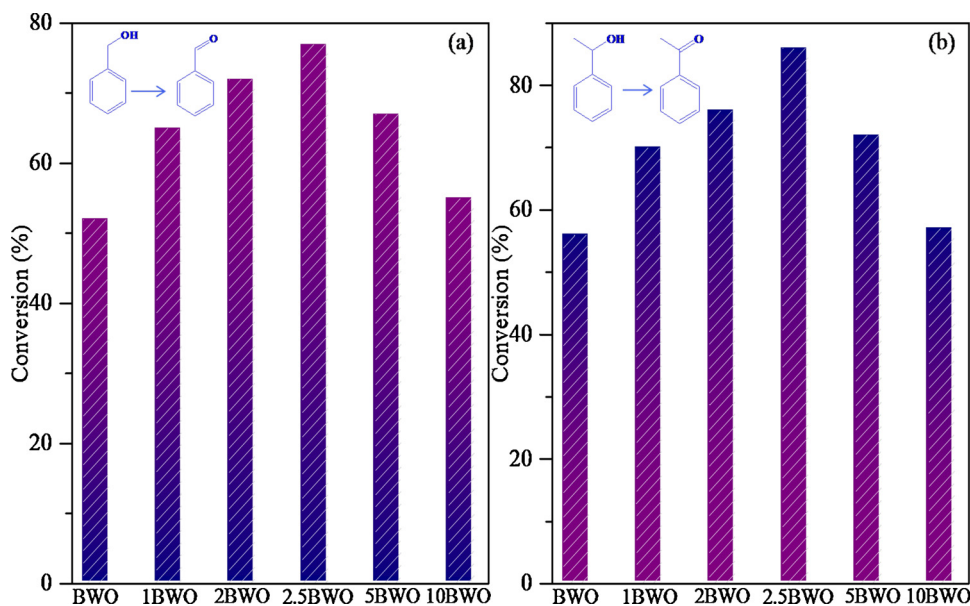


Fig. 10. Photocatalytic performances of different catalysts for selective oxidation of benzyl alcohol (a) and 1-phenylethanol (b).

previous researches [8–10,67]. This appearance could be attributed to the reason that the electron-donating groups endowed the $-CH_2OH$ and $-CHOH-CH_3$ moieties with higher electron cloud density than those with electron-withdrawing groups and thus, the photogenerated holes could much more easily activate and react with the $-CH_2OH$ and $-CHOH-CH_3$ moieties to generate their corresponding cation radicals, which also further validated the rationality about the photocatalytic reaction mechanism for selective oxidation of aromatic alcohols to carbonyl compounds as proposed in Scheme 1.

The durability of photocatalysts is a very important reference criterion for their potential in practical applications. For evaluating the durability, the 2.5BWO as the optimal photocatalyst in this study was selected to explore the durability in the recycled photocatalytic selective oxidations of benzyl alcohol and 1-phenylethanol. The 2.5BWO was completely separated from the reaction solution by centrifugation after each photocatalytic reaction, and then thoroughly washed with

absolute ethanol and distilled water for three times. Each photocatalytic selective oxidation reaction was carried out by recharging fresh reagents into the recycled 2.5BWO for guaranteeing each photocatalytic reaction under the identical conditions. From Fig. 12, it was obvious that the 2.5BWO could be reused at least five times and no significant deactivation in photocatalytic activities for selective oxidations of benzyl alcohol and 1-phenylethanol were observed, showing its excellent durability and good potential in practical applications. The excellent durability of 2.5BWO could be mainly associated with the strong interaction between metallic Bi particles and robust Bi_2WO_{6-x} nanosheets, which restrained the significant deactivation caused by either the leaching of metallic Bi particles or the structural collapse of Bi_2WO_{6-x} nanosheets since the morphological structures of 2.5BWO remained almost intact after the fifth recycling test (see Fig. S3).

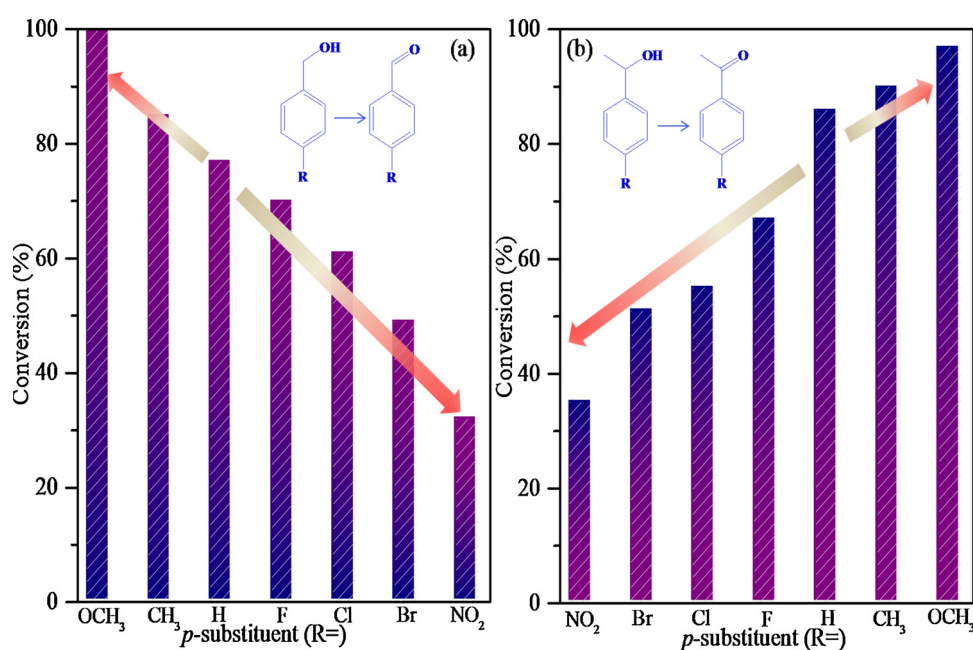


Fig. 11. Photocatalytic performances for selective oxidation of benzylic alcohols (a) and 1-phenylethanols (b) with different *p*-substituents over 2.5BWO.

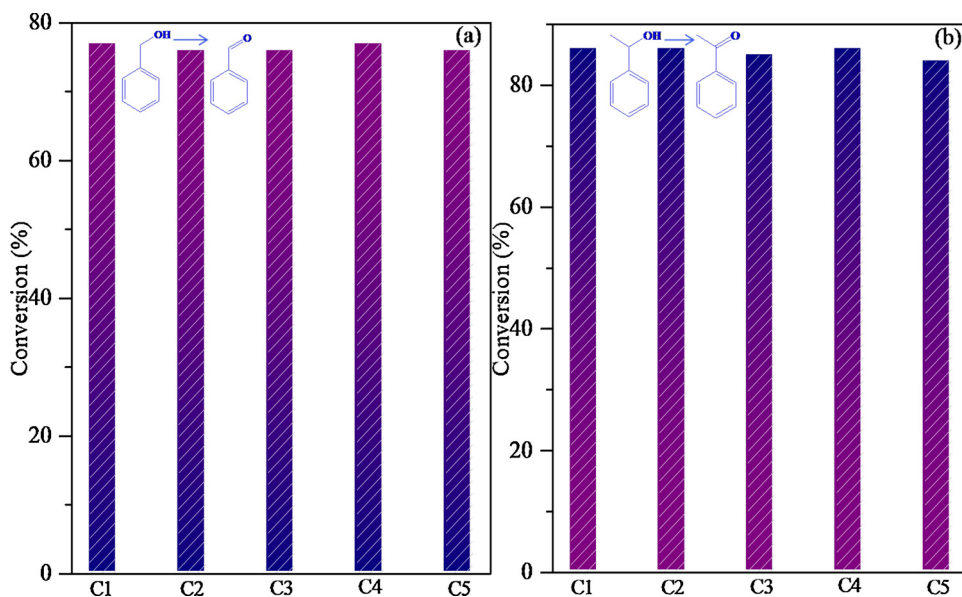


Fig. 12. Stability test of 2.5BWO for selective oxidation of benzyl alcohol (a) and 1-phenylethanol (b).

4. Conclusions

In summary, this work developed a facile strategy for synthesizing $\text{Bi}_2\text{WO}_{6-x}$ nanosheets with tunable Bi quantum dots and oxygen vacancies, which exhibited the remarkably enhanced activity for selective oxidation of aromatic alcohols to carbonyl compounds in aqueous medium under visible-light irradiation. The remarkably enhanced activity of this photocatalyst was mainly originated from the synergistic effect of Bi quantum dots and oxygen vacancies that resulted in the energy band gap narrowing, the enhanced light-harvesting ability and the improved separation efficiency of photoelectron-hole pairs. This photocatalyst also presented excellent durability due to the strong interaction between Bi quantum dots and robust $\text{Bi}_2\text{WO}_{6-x}$ nanosheets against significant deactivation caused by either the leaching of Bi quantum dots or the structural collapse of $\text{Bi}_2\text{WO}_{6-x}$ nanosheets, showing its good potential in practical applications. This work can deliver some new insights for guiding the rational design of high-efficient semiconductor photocatalysts applied in the field of green and sustainable organic transformations.

Acknowledgements

This work is supported by Shanghai Talent Development Foundation (2017076), Shanghai Municipal Education Commission (ZZGCD15031), Shanghai Key Laboratory of Rare Earth Functional Materials (2018No.01), National Natural Science Foundation of China (21503133), Shanghai Government (17SG44) and the Talent Program of Shanghai University of Engineering Science.

Appendix A. Supplementary data

Supplementary material related to this article can be found, in the online version, at doi:<https://doi.org/10.1016/j.apcatb.2019.117874>.

References

- [1] Y.B. Kuang, N.M. Islam, Y. Nabae, T. Hayakawa, M. Kakimoto, Selective aerobic oxidation of benzylic alcohols catalyzed by carbon-based catalysts: a nonmetallic oxidation system, *Angew. Chem. Int. Ed.* **49** (2010) 436–440.
- [2] C. Aellig, C. Girard, I. Hermans, Aerobic alcohol oxidations mediated by nitric acid, *Angew. Chem. Int. Ed.* **50** (2011) 12355–12360.
- [3] I. Tamiolakis, I.N. Lykakis, C.D. Malliakas, G.S. Armatas, Ordered mesoporous Cr_2O_3 frameworks incorporating keggin-type 12-phosphotungstic acids as efficient catalysts for oxidation of benzyl alcohols, *J. Mater. Chem.* **22** (2012) 6919–6927.
- [4] J.J. Zhu, Y.X. Zhao, D.H. Tang, Z. Zhao, A.C. Carabineiro, Aerobic selective oxidation of alcohols using $\text{La}_{1-x}\text{Ce}_x\text{CoO}_3$ perovskite catalysts, *J. Catal.* **340** (2016) 41–48.
- [5] J. Wang, X.J. Lang, B. Zhao, M.L. Jia, J. Wang, X.F. Guo, J.C. Zhao, Aerobic oxidation of alcohols on Au nanocatalyst: insight to the roles of the Ni-Al layered double hydroxides support, *ChemCatChem* **6** (2014) 1737–1747.
- [6] Y.W. Feng, H. Li, L.L. Ling, S. Yan, D.L. Pan, H. Ge, H.X. Li, Z.F. Bian, Enhanced photocatalytic degradation performance by fluid-induced piezoelectric field, *Environ. Sci. Technol.* **52** (2018) 7842–7848.
- [7] Y.W. Feng, L.L. Ling, J.H. Nie, K. Han, X.Y. Chen, Z.F. Bian, H.X. Li, Z.L. Wang, Self-powered electrostatic filter with enhanced photocatalytic degradation of formaldehyde based on built-in triboelectric nanogenerators, *ACS Nano* **11** (2017) 12411–12418.
- [8] X.R. Li, J.G. Wang, Y. Men, Z.F. Bian, TiO_2 mesocrystal with exposed (001) facets and CdS quantum dots as an active visible photocatalyst for selective oxidation reactions, *Appl. Catal. B* **187** (2016) 115–121.
- [9] Z.M. Chen, J.G. Wang, G.J. Zhai, W. An, Y. Men, Hierarchical yolk-shell WO_3 microspheres with highly enhanced photoactivity for selective alcohol oxidations, *Appl. Catal. B* **218** (2017) 825–832.
- [10] J.G. Wang, Z.M. Chen, G.J. Zhai, Y. Men, Boosting photocatalytic activity of WO_3 nanorods with tailored surface oxygen vacancies for selective alcohol oxidations, *Appl. Surf. Sci.* **462** (2018) 760–771.
- [11] B. Zhang, J. Li, Y.Y. Gao, R.F. Chong, Z.L. Wang, L. Guo, X.W. Zhang, C. Li, To boost photocatalytic activity in selective oxidation of alcohols on ultrathin Bi_2MoO_6 nanoplates with Pt nanoparticles as cocatalyst, *J. Catal.* **345** (2017) 96–103.
- [12] S.J. Liang, L.R. Wen, S. Lin, J.H. Bi, P.Y. Feng, X.Z. Fu, L. Wu, Monolayer HNB_3O_8 for selective photocatalytic oxidation of benzylic alcohols with visible light response, *Angew. Chem. Int. Ed.* **53** (2014) 2951–2955.
- [13] M.C. Wen, G.Y. Li, H.L. Liu, J.Y. Chen, T.C. An, H. Yamashita, Metal-organic framework-based nanomaterials for adsorption and photocatalytic degradation of gaseous pollutants: recent progress and challenges, *Environ. Sci. Nano* **6** (2019) 1006–1025.
- [14] M.C. Wen, K. Mori, Y. Kuwahara, T.C. An, H. Yamashita, Design of single-site photocatalysts by using metal-organic frameworks as a matrix, *Chem.-Asian J.* **13** (2018) 1767–1779.
- [15] H.X. Li, Z.F. Bian, J. Zhu, Y.N. Huo, H. Li, Y.F. Lu, Mesoporous Au/TiO_2 nanocomposites with enhanced photocatalytic activity, *J. Am. Chem. Soc.* **129** (2007) 4538–4539.
- [16] Z.M. Xu, R. Zheng, Y. Chen, J. Zhu, Z.F. Bian, Ordered mesoporous Fe/TiO_2 with light enhanced photo-Fenton activity, *Chin. J. Catal.* **40** (2019) 631–637.
- [17] L.L. Ling, Y.W. Feng, H. Li, Y. Chen, J.Y. Wen, J. Zhu, Z.F. Bian, Microwave induced surface enhanced pollutant adsorption and photocatalytic degradation on Ag/TiO_2 , *Appl. Surf. Sci.* **483** (2019) 772–778.
- [18] E. Grabowska, J.W. Sobczak, M. Gazda, A. Zalesk, Surface properties and visible light activity of $\text{W}-\text{TiO}_2$ photocatalysts prepared by surface impregnation and sol-gel method, *Appl. Catal. B* **117–118** (2012) 351–359.
- [19] Y.X. Zhang, M.J. Xu, H. Li, H. Ge, Z.F. Bian, The enhanced photoreduction of $\text{Cr}(\text{VI})$ to $\text{Cr}(\text{III})$ using carbon dots coupled TiO_2 mesocrystals, *Appl. Catal. B* **226** (2018) 213–219.
- [20] R. Asahi, T. Morikawa, H. Irie, T. Ohwaki, Nitrogen-doped titanium dioxide as visible-light-sensitive photocatalyst: designs, developments, and prospects, *Chem. Rev.* **114** (2014) 9824–9852.
- [21] H.X. Li, X.Y. Zhang, Y.N. Huo, J. Zhu, Supercritical preparation of a highly active S-doped TiO_2 photocatalyst for methylene blue mineralization, *Environ. Sci. Technol.*

41 (2007) 4410–4414.

[22] N. Zhang, Y.H. Zhang, X.Y. Pan, X.Z. Fu, S.Q. Liu, Y.J. Xu, Assembly of CdS nanoparticles on the two-dimensional graphene scaffold as visible-light-driven photocatalyst for selective organic transformation under ambient conditions, *J. Phys. Chem. C* 115 (2011) 23501–23511.

[23] Y.P. Bi, S. Ouyang, N. Umezawa, J.Y. Cao, J.H. Ye, Facet effect of single-crystalline Ag_3PO_4 submicro-crystals on photocatalytic properties, *J. Am. Chem. Soc.* 133 (2011) 6490–6492.

[24] X.C. Wang, K. Maeda, A. Thomas, K. Takanabe, G. Xin, J.M. Carlsson, K. Domen, M. Antonietti, A metal-free polymeric photocatalyst for hydrogen production from water under visible light, *Nat. Mater.* 8 (2009) 76–80.

[25] J.G. Hou, C. Yang, Z. Wang, W.L. Zhou, S.Q. Jiao, H.M. Zhu, In situ synthesis of α - β phase heterojunction on Bi_2O_3 nanowires with exceptional visible-light photocatalytic performance, *Appl. Catal. B* 142–143 (2013) 504–511.

[26] J.P. Wang, Y.A. Song, J. Hu, Y. Li, Z.Y. Wang, P. Yang, G. Wang, Q. Ma, Q.D. Che, Y. Dai, B.B. Huang, Photocatalytic hydrogen evolution on P-type tetragonal zircon BiVO_4 , *Appl. Catal. B* 251 (2019) 94–101.

[27] K.Q. Jing, W. Ma, Y.H. Ren, J.H. Xiong, B.B. Guo, Y.J. Song, S.J. Liang, L. Wu, Hierarchical Bi_2MoO_6 spheres in situ assembled by monolayer nanosheets toward photocatalytic selective oxidation of benzyl alcohol, *Appl. Catal. B* 243 (2019) 10–18.

[28] C. Zhang, Y.F. Zhu, Synthesis of square Bi_2WO_6 nanoplates as high-activity visible-light-driven photocatalysts, *Chem. Mater.* 17 (2005) 3537–3545.

[29] S.M. Sun, W.Z. Wang, J.H. Xu, L. Wang, Z.J. Zhang, Highly efficient photocatalytic oxidation of phenol over ordered mesoporous Bi_2WO_6 , *Appl. Catal. B* 106 (2011) 559–564.

[30] Z.Y. Jiang, X.Z. Liang, H.L. Zheng, Y.Y. Liu, Z. Wang, P. Wang, X.Y. Zhang, X.Y. Qin, Y. Dai, M.H. Whangbo, B.B. Huang, Photocatalytic reduction of CO_2 to methanol by three-dimensional hollow structures of Bi_2WO_6 quantum dots, *Appl. Catal. B* 219 (2017) 209–215.

[31] M. Zargazi, M.H. Entezari, Anodic electrophoretic deposition of Bi_2WO_6 thin film: high photocatalytic activity for degradation of a binary mixture, *Appl. Catal. B* 242 (2019) 507–517.

[32] J. Zhu, J.G. Wang, Z.F. Bian, F.L. Cao, H.X. Li, Solvothermal synthesis of highly active Bi_2WO_6 visible photocatalyst, *Res. Chem. Intermed.* 35 (2009) 799–806.

[33] J.J. Yang, D.M. Chen, Y. Zhu, Y.M. Zhang, Y.F. Zhu, 3D-3D porous Bi_2WO_6 /graphene hydrogel composite with excellent synergistic effect of adsorption-enrichment and photocatalytic degradation, *Appl. Catal. B* 205 (2017) 228–237.

[34] X.F. Qian, D.T. Yue, Z.Y. Tian, M. Reng, Y. Zhu, M. Kan, T.Y. Zhang, Y.X. Zhao, Carbon quantum dots decorated Bi_2WO_6 nanocomposite with enhanced photocatalytic oxidation activity for VOCs, *Appl. Catal. B* 193 (2016) 16–21.

[35] Y.Y. Wang, W.J. Jiang, W.J. Luo, X.J. Chen, Y.F. Zhu, Ultrathin nanosheets g- C_3N_4 @ Bi_2WO_6 core-shell structure via low temperature reassembled strategy to promote photocatalytic activity, *Appl. Catal. B* 237 (2018) 633–640.

[36] G.M. Wang, Y. Yang, D.D. Han, Y. Li, Oxygen defective metal oxides for energy conversion and storage, *Nano Today* 13 (2017) 23–39.

[37] W. Zhou, H.G. Fu, Defect-mediated electron-hole separation in semiconductor photocatalysis, *Inorg. Chem. Front.* 5 (2018) 1240–1254.

[38] H. Li, J. Li, Z.H. Ai, F.L. Jia, L.Z. Zhang, Oxygen vacancy-mediated photocatalysis of BiOCl : reactivity, selectivity, and perspectives, *Angew. Chem. Int. Ed.* 57 (2018) 122–138.

[39] H. Li, J.G. Shi, K. Zhao, L.Z. Zhang, Sustainable molecular oxygen activation with oxygen vacancies on the {001} facets of BiOCl nanosheets under solar light, *Nanoscale* 6 (2014) 14168–14173.

[40] M.J. Xu, Y. Chen, J.T. Qin, Y.W. Feng, W. Li, W. Chen, J. Zhu, H.X. Li, Z.F. Bian, Unveiling the role of defects on oxygen activation and photodegradation of organic pollutants, *Environ. Sci. Technol.* 52 (2018) 13879–13886.

[41] X.Y. Kong, Y.Y. Choo, S.P. Chai, A.K. Soh, A.R. Mohamed, Oxygen vacancies induced Bi_2WO_6 for realization of full solar spectrum photocatalytic CO_2 reduction: from UV to NIR region, *Chem. Commun.* 52 (2016) 14242–14245.

[42] J.G. Hou, S.Y. Cao, Y.Z. Wu, F. Liang, Y.F. Sun, Z.S. Lin, L.C. Sun, Simultaneously efficient light absorption and charge transport of phosphate and oxygen-vacancy confined in bismuth tungstate atomic layers triggering robust solar CO_2 reduction, *Nano Energy* 32 (2017) 359–366.

[43] Z.J. Zhang, W.Z. Wang, E.P. Gao, M. Shang, J.H. Xu, Enhanced photocatalytic activity of Bi_2WO_6 with oxygen vacancies by zirconium doping, *J. Hazard. Mater.* 196 (2011) 255–262.

[44] Y.H. Lv, W.Q. Yao, R.L. Zong, Y.F. Zhu, Fabrication of wide-range-visible photocatalyst $\text{Bi}_2\text{WO}_{6-x}$ nanoplates via surface oxygen vacancies, *Sci. Rep.* 6 (2016) 19347.

[45] W.C. Huo, X. Dong, J.Y. Li, M. Liu, X.Y. Liu, Y.X. Zhang, F. Dong, Synthesis of Bi_2WO_6 with gradient oxygen vacancies for highly photocatalytic NO oxidation and mechanism study, *Chem. Eng. J.* 361 (2019) 129–138.

[46] J.Q. Li, Z. Liang, Y. Qin, L. Guo, N. Lei, Q.Q. Song, Defective Bi_2WO_6 -supported Cu nanoparticles as efficient and stable photoelectrocatalytic for water splitting in near-neutral media, *Energy Technol.* 6 (2018) 2247–2255.

[47] J. Yang, X.H. Wang, Y.M. Chen, J. Dai, S.H. Sun, Enhanced photocatalytic activities of visible-light driven green synthesis in water and environmental remediation on Au/ Bi_2WO_6 hybrid nanostructures, *RSC Adv.* 5 (2015) 9771–9782.

[48] D. Sun, Y. Le, C.J. Jiang, B. Cheng, Ultrathin Bi_2WO_6 nanosheet decorated with Pt nanoparticles for efficient formaldehyde removal at room temperature, *Appl. Surf. Sci.* 441 (2018) 429–437.

[49] Q.S. Wu, Y. Cui, L.M. Yang, G.Y. Zhang, D.Z. Gao, Facile in-situ photocatalysis of Ag/ Bi_2WO_6 heterostructure with obviously enhanced performance, *Sep. Purif. Technol.* 142 (2015) 168–175.

[50] R.A. He, S.W. Cao, P. Zhou, J.G. Yu, Recent advances in visible light Bi-based photocatalysts, *Chin. J. Catal.* 35 (2014) 989–1007.

[51] Y.K. Huang, S.F. Kang, Y. Yang, H.F. Qin, Z.J. Ni, S.J. Yang, X. Li, Facile synthesis of Bi/ Bi_2WO_6 nanocomposite with enhanced photocatalytic activity under visible light, *Appl. Catal. B* 196 (2016) 89–99.

[52] S.X. Yu, Y.H. Zhang, M. Li, X. Du, H.W. Huang, Non-noble metal Bi deposition by utilizing Bi_2WO_6 as the self-sacrificing template for enhancing visible light photocatalytic activity, *Appl. Surf. Sci.* 391 (2017) 491–498.

[53] J.Y. Gong, A. Imbault, R. Farnood, The promoting role of bismuth for the enhanced photocatalytic oxidation of lignin on Pt-TiO₂ under solar light illumination, *Appl. Catal. B* 204 (2017) 296–303.

[54] X.W. Liu, H.Q. Cao, J.F. Yin, Generation and photocatalytic activities of Bi@ Bi_2O_3 microspheres, *Nano Res.* 4 (2011) 470–482.

[55] Y. Yu, C.Y. Cao, H. Liu, P. Li, F.F. Wei, Y. Jiang, W.G. Song, A Bi/BiOCl heterojunction photocatalyst with enhanced electron-hole separation and excellent visible light photodegrading activity, *J. Mater. Chem. A* 2 (2014) 1677–1681.

[56] F. Dong, Q.Y. Li, Y.J. Sun, W.K. Ho, Noble metal-like behavior of plasmonic Bi particles as a cocatalyst deposited on ($\text{BiO})_2\text{CO}_3$ microspheres for efficient visible light photocatalysis, *ACS Catal.* 4 (2014) 4341–4350.

[57] S.F. Yang, J.G. Wang, W. Chai, J. Zhu, Y. Men, Enhanced soot oxidation activity over CuO/CeO_2 mesoporous nanosheets, *Catal. Sci. Technol.* 9 (2019) 1699–1709.

[58] G.J. Zhai, J.G. Wang, Z.M. Chen, S.F. Yang, Y. Men, Highly enhanced soot oxidation activity over 3DOM $\text{Co}_3\text{O}_4/\text{CeO}_2$ catalysts by synergistic promoting effect, *J. Hazard. Mater.* 363 (2019) 214–226.

[59] C. Zhang, J.G. Wang, S.F. Yang, H. Liang, Y. Men, Boosting total oxidation of acetone over spinel MCo_2O_4 ($\text{M} = \text{Co}, \text{Ni}, \text{Cu}$) hollow mesoporous spheres by cation-substituting effect, *J. Colloid Interface Sci.* 539 (2019) 65–75.

[60] Y. Liu, B. Wei, L.L. Xu, H. Gao, M.Y. Zhang, Generation of oxygen vacancy and OH radicals: a comparative study of Bi_2WO_6 and $\text{Bi}_2\text{WO}_{6-x}$ nanoplates, *ChemCatChem* 7 (2015) 4076–4084.

[61] S.S. Zhang, W.H. Pu, H. Du, Y.Y. Wang, C.Z. Yang, J.Y. Gong, Facile synthesis of Pt assisted $\text{Bi}-\text{Bi}_2\text{WO}_{6-x}$ with oxygen vacancies for the improved photocatalytic activity under visible light, *Appl. Surf. Sci.* 459 (2018) 363–375.

[62] L.L. Ji, B. Li, X.T. Xu, F. Wang, Oxygen deficiencies and metallic Bi-mediated photocatalytic activity of bismuth tungsten oxides, *Appl. Surf. Sci.* 463 (2019) 872–878.

[63] G.J. Zhai, J.G. Wang, Z.M. Chen, W. An, Y. Men, Boosting soot combustion efficiency of Co_3O_4 nanocrystals via tailoring crystal facets, *Chem. Eng. J.* 337 (2018) 488–498.

[64] J.G. Wang, P. Zhang, X. Li, J. Zhu, H.X. Li, Synchronical pollutant degradation and H_2 production on a Ti^{3+} -doped TiO_2 visible photocatalyst with dominant (001) facets, *Appl. Catal. B* 134–135 (2013) 198–204.

[65] C.L. Cai, J.G. Wang, F.L. Cao, H.X. Li, J. Zhu, Synthesis and photocatalytic activity of F/TiO_2 nanocrystals with exposed (001) facets via a nonhydrolytic solvothermal route, *Chin. J. Catal.* 32 (2011) 862–871.

[66] H.B. Yin, Y. Kuwahara, K. Mori, H. Yamashita, Plasmonic metal/ $\text{Mo}_{x}\text{W}_{1-x}\text{O}_3$ for visible-light-enhanced H_2 production from ammonia borane, *J. Mater. Chem. A* 6 (2018) 10932–10938.

[67] J.G. Wang, P.H. Rao, W. An, J.L. Xu, Y. Men, Boosting photocatalytic activity of Pd decorated TiO_2 nanocrystal with exposed (001) facets for selective alcohol oxidations, *Appl. Catal. B* 195 (2016) 141–148.

[68] J.G. Wang, Z.F. Bian, J. Zhu, H.X. Li, Ordered mesoporous TiO_2 with exposed (001) facets and enhanced activity in photocatalytic selective oxidation of alcohols, *J. Mater. Chem. A* 1 (2013) 1296–1302.